Quantized crossed Andreev reflection in altermagnet/altermagnet topological superconductor/altermagnet heterojunction

Xing Wang,[1,2,3] Kai-Yi Lyu,[1] Yong Guo,[2,3] and Yu-Xian Li[1,*]

[1]*College of Physics and Hebei Advanced Thin Films Laboratory, Hebei Normal University, Shijiazhuang, Hebei 050024, People's Republic of China*

[2]*Department of Physics, Tsinghua University, Beijing 100084, People's Republic of China*

[3]*State Key Laboratory of Low-Dimensional Quantum Physics, Tsinghua University, Beijing 100084, People's Republic of China*

(Received 5 August 2025; accepted 12 December 2025; published 6 January 2026)

We propose an altermagnet/altermagnet topological superconductor/altermagnet (AM/AMTSC/AM) heterojunction exhibiting a filtering effect, where the vast majority of incident electrons are locally reflected, and only a small portion passes through the center region of the AMTSC. Within an appropriate parameter range, the AMTSC hosts chiral Majorana edge states (CMES), causing the transmission coefficient and the crossed Andreev reflection coefficient of the heterojunction to remain equal and exhibit quantized plateaus. By tuning system parameters, the number of CMES can be changed, thereby controlling the plateau values to be 1/2, 1/4, or 0. When the system has anisotropy, the plateaus corresponding to the AMTSC with s-wave pairing and $s + s_{\pm}$-wave pairing exhibit different variation trends. In the absence of anisotropy, quantized plateaus can also appear for the $s + d$-wave pairing. Moreover, the chemical potential and the spin polarization orientation angle of the AM can also adjust the plateau values and enrich these variations. All these phenomena originate from the CMES in the AMTSC and the tunneling between them, which exhibit strong robustness against disorder and can work stably over a wide range of system parameters.

DOI: 10.1103/rv94-djlk

I. INTRODUCTION

Recently, altermagnetism has attracted much attention in the field of condensed matter physics [1–6]. Altermagnets (AMs) exhibits zero net magnetization, similarly to antiferromagnets, due to the alternating order of magnetic moments in direct space. However, it also exhibits an alternating spin-polarized order in momentum space, resembling that of ferromagnets, which results in the breaking of time-reversal symmetry. Therefore, altermagnetism is regarded as the third magnetic phase after ferromagnetism and antiferromagnetism [7,8]. Currently, dozens of materials are proposed to exhibit altermagnetic order [9]. Among them, RuO_2, Mn_5Si_3, MnF_2, and MnO_2 are among the most studied d-wave altermagnets. As an AM possesses zero net macroscopic magnetization, it is an ideal material with great advantages for designing and constructing superconducting heterostructures. In addition, the crystal orientation of an AM significantly affects the transport properties of heterojunctions [5,10–14]. This is mainly due to the anisotropic spin polarization within the AM, which enhances the tunability of the system.

Topological superconductors (TSCs) have attracted researchers' interest due to their ability to host Majorana fermions in condensed matter systems [15–18]. Majorana fermions possess non-Abelian statistics and nonlocal properties, so they are regarded as the basic building blocks for quantum computation [19–21]. So far, several material systems have been proposed to realize such states [22–25]. Very recently, topological superconducting phases and Majorana edge and corner states have been observed in AMs with Rashba spin-orbit coupling (RSOC) and in heterostructures formed by AMs and two-dimensional topological insulators [26,27]. Traditional platforms usually rely on external magnetic fields or ferromagnets to break time-reversal symmetry, but this often suppresses the superconducting gap. Moreover, disorder can induce trivial zero-energy states that are difficult to distinguish from the protected Majorana zero modes (MZMs). In contrast, an altermagnet topological superconductor (AMTSC) itself has zero net magnetization and can spontaneously break time-reversal symmetry, effectively avoiding the suppression of the superconducting gap caused by external magnetic fields. Moreover, the AMTSC allows for differentiation between subgap modes and topological MZMs through the application of a Zeeman field [28]. These unique advantages make the AMTSC a highly promising system for achieving stable and controllable topological superconductivity and Majorana states.

Andreev reflection (AR) is a process of electron-hole conversion occurring at the interface between a superconductor and a conductor [29], where an incident electron is converted into a hole while a Cooper pair is simultaneously formed inside the superconductor. Local Andreev reflection (LAR) refers to the process in which the electron and reflected hole are at the same lead [30–32], while crossed Andreev reflection (CAR) is a nonlocal process in which the electron and hole

*Contact author: yxli@mail.hebtu.edu.cn

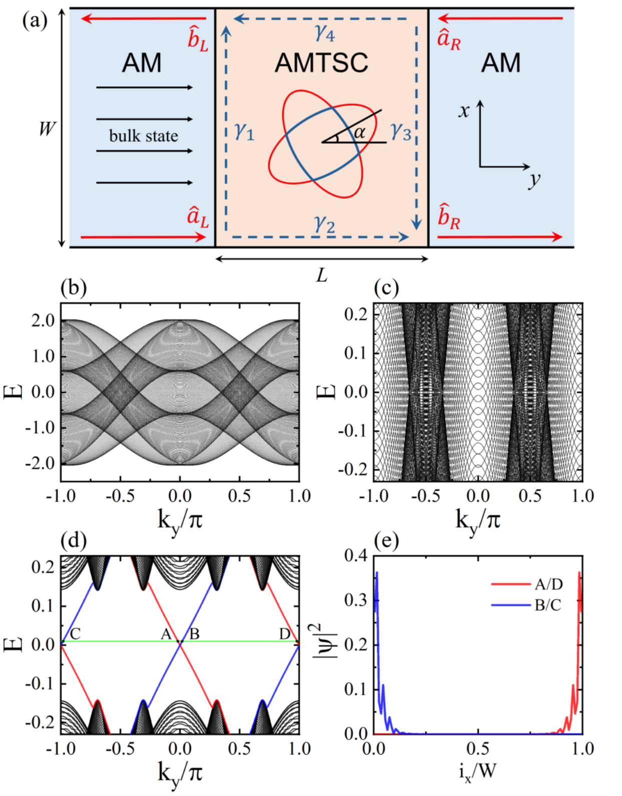

FIG. 1. (a) Schematic diagram of the AM/AMTSC/AM junction. The center region is the AMTSC with length L and width W, and the left and right leads are semi-infinite AMs. The two ellipses represent the Fermi surfaces of different spin electrons in the AMs with RSOC at an orientation angle α, which is defined as the angle between the AM crystal axis and the interface normal. Here, the blue lines represent down-spin electrons, and the red lines represent up-spin electrons. The black arrows in the left AM region represent the incident bulk states. $\hat{a}_{L/R}$ and $\hat{b}_{L/R}$ represents the incident and outgoing particles in the left/right regions, respectively, which are indicated by red arrows. γ_1–γ_4 represent the CMES, which are indicated by blue dashed arrows. (b) Energy band structure of the AMs in the left and right regions. Here, $b_1 = 1$, $\mu = 0$, $\alpha = 0$. (c) An enlarged view of plot (b). (d) Energy band structure of the s-wave AMTSC in the center region. The red and blue lines are the Majorana edge states. Here, $\Delta_0 = 0.3$, $\Delta_1 = 0$; other parameters are the same as in plot (b). (e) Distribution of edge states along the sample cross section in the center region, where A, B, C, and D correspond to the points in (d).

are located at two spatially separated leads [33–35]. Through CAR, Cooper pairs can be spatially separated. These spatially separated and entangled electrons constitute key building blocks in quantum communication and quantum computing [36–38]. Recent studies have shown that CAR can be effectively enhanced in superconducting heterostructures based on AMs [39]. Moreover, the transport properties of the junction are mainly determined by the AR when the bias voltage is below the superconducting gap [40–42].

Based on this, we propose an AM/AMTSC/AM junction as shown in Fig. 1(a). It is found that the heterojunction exhibits a filtering effect, where the vast majority of incident electrons are locally reflected, and only a small fraction can pass through the center region of the AMTSC. Within an appropriate parameter range, the transmission coefficient and the CAR coefficient remain equal and exhibit quantized plateaus. Moreover, system parameters can also adjust the plateau values and enrich these variations. All these phenomena originate from the chiral Majorana edge states (CMES) in the AMTSC and the tunneling between them. The rest of the paper is organized as follows. In Sec. II, we introduce the Hamiltonians and energy bands of AM and AMTSC, along with the formulas and methods used to calculate the transmission coefficient and Andreev rection coefficient. The numerical results are discussed in Sec. III. Finally, a brief summary is drawn in Sec. IV.

II. MODEL AND METHODS

The AM/AMTSC/AM junction we considered as shown in Fig. 1(a). The finite width along the x direction of the junction is W. The length of AMTSC in the center region is L. The semi-infinite AM leads are placed in the left and right regions, respectively. The Hamiltonian of this hybrid device is written as $H = H_C + H_{L/R} + H_T$, where H_C, $H_{L/R}$, and H_T are the Hamiltonians of the AMTSC, AM, and the coupling between them, respectively.

The Bogoliubov–de Gennes (BdG) Hamiltonian for the AMTSC in the center region can be written as [28,43]

$$H_C^0(\mathbf{k}) = H_0(\mathbf{k}) + H_J(\mathbf{k}) + H_\lambda(\mathbf{k}) + H_\Delta(\mathbf{k}), \tag{1}$$

where $H_0(\mathbf{k}) = [t(\cos k_x + b_1 \cos k_y) - \mu]\tau_z \otimes \sigma_0$, $H_J(\mathbf{k}) = J_A(\cos k_x - \cos k_y)\tau_z \otimes \sigma_z$, $H_\lambda(\mathbf{k}) = \lambda_R(\sin k_x \tau_z \otimes \sigma_y - \sin k_y \tau_0 \otimes \sigma_x)$, and $H_\Delta(\mathbf{k}) = [\Delta_0 + \Delta_1(\cos k_x + b_3 \cos k_y)]\tau_y \otimes \sigma_y$ describe the kinetic energy of particles, the d-wave altermagnetism, the spin-orbit coupling, and the superconductivity, respectively. Here, $\mathbf{k} = (k_x, k_y)$ is the wave vector, t is the hopping energy, and μ is the chemical potential. J_A and λ_R are the magnitudes of altermagnetism and Rashba spin-orbit coupling. The parameters b_1 and b_3 represent anisotropic distortions along the y direction for hopping and superconducting strength, respectively. They can break the system's symmetry, causing a transition from a weak topological phase to a strong topological phase with a nonzero Chern number, and simultaneously changing the number of topological edge states. The anisotropy of other terms does not qualitatively change the results. Thus, to simplify the model and maintain zero net magnetization, these anisotropies are not considered. In practice, anisotropy can be altered through methods such as strain engineering, chemical doping, external electric or magnetic fields, and substrate choice [44–48]. Δ_0 and Δ_1 are the superconducting pairing amplitudes. The case when $\Delta_0 \neq 0$ and $\Delta_1 = 0$ corresponds to s-wave pairing. When $\Delta_0, \Delta_1 \neq 0$, $b_3 > 0$ corresponds to $s + s_\pm$-wave pairing, while $b_3 < 0$ corresponds to $s + d$-wave pairing [28]. $\tau_{x,y,z,0}$ and $\sigma_{x,y,z,0}$ are the Pauli matrices in particle-hole space and spin space, respectively.

Next, we introduce different orientation angles α in the system, which is defined as the angle between the AM crystal axis and the interface normal [see Fig. 1(a)]. The Hamiltonian of the AMTSC corresponding to the system rotated by an angle α about the z axis is $H_C(\mathbf{k}) = H_C^0(U_z(\alpha)\mathbf{k})$, where $U_z(\alpha) = \left(\begin{smallmatrix} \cos\alpha & \sin\alpha \\ -\sin\alpha & \cos\alpha \end{smallmatrix}\right)$ is the rotation operator. Different orientation angles α can be obtained through methods such as appropriate sample cutting, epitaxial growth, and mechanical stacking [11,49–51].

Then we discretize the Hamiltonian on a two-dimensional square lattice with the lattice constant $a = 1$, and perform Fourier transformation along the x and y directions to obtain the discretized Hamiltonian. For the semi-infinite AM leads in the left and right regions, the difference between their Hamiltonian and that of the center region lies the absence of the superconductivity term. Moreover, the coupling between the AM leads and the center region is perfect (see Supplemental Material (SM) part A [52] for the specific forms of the discrete Hamiltonian).

The energy band structures of the AM and AMTSC, and the distribution of edge states along the sample cross section in the center region, are shown in Figs. 1(b)–1(e). In the AM region, the absence of band gap in the bulk states results in a large number of channels near the incident energy $E = 0$ [see Figs. 1(b) and 1(c)]. In the AMTSC region, two pairs of CMES are present, which transport in the same direction on the same boundary [see Figs. 1(d) and 1(e)].

Next, based on the Landauer-Büttiker formula combined with the non-equilibrium Green's function method, the transmission coefficient T, the local Andreev reflection coefficient $T_{\rm LAR}$, and the cross Andreev reflection coefficient $T_{\rm CAR}$ of the AM/AMTSC/AM junction can be obtained as [42,53,54] $T(E) = {\rm Tr}[\Gamma^L_{ee} G^r_{ee} \Gamma^R_{ee} G^a_{ee}]$, $T_{\rm LAR}(E) = {\rm Tr}[\Gamma^L_{ee} G^r_{eh} \Gamma^L_{hh} G^a_{he}]$, $T_{\rm CAR}(E) = {\rm Tr}[\Gamma^L_{ee} G^r_{eh} \Gamma^R_{hh} G^a_{he}]$, where E is the incident energy,and $\Gamma^\beta(E) = i[\Sigma^r_\beta(E) - \Sigma^a_\beta(E)]$ is the linewidth function of the β lead. The Green's function $G^r(E) = [G^a(E)]^\dagger = [E\mathbf{I} - H_{\rm cen} - \Sigma^r_L - \Sigma^r_R]^{-1}$, with $H_{\rm cen}$ being the Hamiltonian of the center scattering region. Σ^r_β (Σ^a_β) is the retarded (advanced) self-energy due to the coupling between the β lead and the center region [53,55]. $\Sigma^r_\beta = \Sigma^{a\dagger}_\beta = H_{C\beta} g^r_\beta H_{\beta C}$, where $H_{C\beta/\beta C}$ are the coupling matrix between the β lead and the center region, and g^r_β is the surface Green's function of the β lead, which can be calculated by using the cyclic iteration method [56,57].

In numerical calculations, we set the hopping energy $t = 1$, the lattice constant $a = 1$, and the magnitudes of altermagnetism and Rashba spin-orbit coupling $J_A = \lambda_R = 0.3$. Here, we chose a relatively large λ_R to make the physical picture clearer. In experiments, when the altermagnet itself has sizable spin-orbit coupling, while maintaining $\lambda_R \ll J_A$, nanowires can be fabricated directly from the altermagnet material, thus enabling a simpler experimental platform [28]. The length and width of the center region are $L = 100a$ and $W = 80a$, respectively.

III. RESULTS AND DISCUSSION

First, the simplest case of the system is studied: That is, without considering crystal anisotropy ($b_1 = 1$), the AMTSC in the center region corresponds to s-wave pairing ($\Delta_0 \neq 0$, $\Delta_1 = 0$), and both the chemical potential μ and the azimuthal angle α are zero. Figure 2 shows the transmission coefficient T, the local Andreev reflection coefficient $T_{\rm LAR}$, and the cross Andreev reflection coefficient $T_{\rm CAR}$ as a function of the incident energy E. It is observable that within the bulk gap (indicated by two green dashed lines) $T_{\rm LAR}$ is very

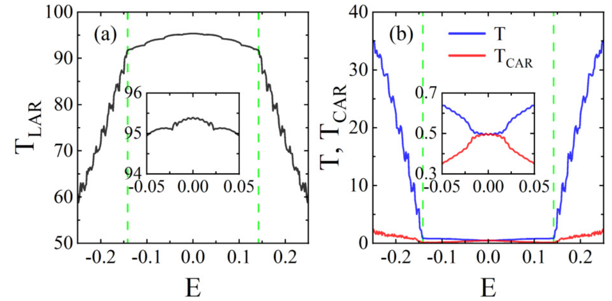

FIG. 2. The local Andreev reflection coefficient $T_{\rm LAR}$, the transmission coefficient T, and the cross Andreev reflection coefficient $T_{\rm CAR}$ as a function of the incident energy E, where $\Delta_0 = 0.3$, $\Delta_1 = 0$, $b_1 = 1$, $\mu = 0$, $\alpha = 0$. The insets in panels are the enlarged views near $E = 0$. The vertical green dashed lines indicate the bulk gap in Fig. 1(d).

large, while both T and $T_{\rm CAR}$ are quite small and exhibit a plateau value of 1/2 near $E = 0$. When E exceeds the bulk gap, electron transmission dominates, $T_{\rm LAR}$ decreases rapidly, and $T_{\rm CAR}$ is still small.

The reason behind these observations is the presence of Majorana edge states in the center region. Due to the absence of the bulk gap at the left AM lead [see Figs. 1(b) and 1(c)], there are a large number of incident channels at $E = 0$. In contrast, the center region has a bulk gap, allowing only two pairs of Majorana edge states to serve as transmission channels. Therefore, almost all of the incident electrons undergo local reflection. Additionally, the longer center region length L not only effectively suppresses the tunneling of incident electrons but also weakens the impact of the inverse proximity effect on the edge state channels [58] (see SM part Appendix B [52] for a discussion on the effects of system size). These reasons lead to the dominance of normal electron reflection and LAR within the bulk gap. Next, we discuss the quantitative behavior of T and $T_{\rm CAR}$. The scattering matrix for the operators $\hat{a}_{L/R}$ and $\hat{b}_{L/R}$ in Fig. 1(a) can be written as (a detailed derivation of the scattering matrix can be found in part C of the SM [52]) [54,59,60]

$$\begin{pmatrix} \hat{b}_{L,k} \\ \hat{b}^\dagger_{L,-k} \\ \hat{b}_{R,k} \\ \hat{b}^\dagger_{R,-k} \end{pmatrix} = \frac{1}{2} \begin{pmatrix} 1 & 1 & 1 & -1 \\ 1 & 1 & -1 & 1 \\ 1 & -1 & 1 & 1 \\ -1 & 1 & 1 & 1 \end{pmatrix} \begin{pmatrix} \hat{a}_{L,k} \\ \hat{a}^\dagger_{L,-k} \\ \hat{a}_{R,k} \\ \hat{a}^\dagger_{R,-k} \end{pmatrix}, \quad (2)$$

where $\hat{a}_{L/R}$ and $\hat{b}_{L/R}$ represent the incident and outgoing particles in the left/right regions, respectively. When a pair of CMES exists, $T = T_{\rm LAR} = T_{\rm CAR} = 1/4$. Since there are two pairs of CMES present in the center region, it follows that $T = T_{\rm CAR} = 1/2$.

To sum up, the AM/AMTSC/AM junction can play a filtering role, that is, the vast majority of incident electrons are locally reflected, and only a small part can pass through the Majorana edge state in the center region. Based on this, the following discussion will focus on the influence of system parameters on T and $T_{\rm CAR}$ at $E = 0$.

Next, we discuss the influence of the chemical potential μ and the orientation angle α on T and $T_{\rm CAR}$. First, we

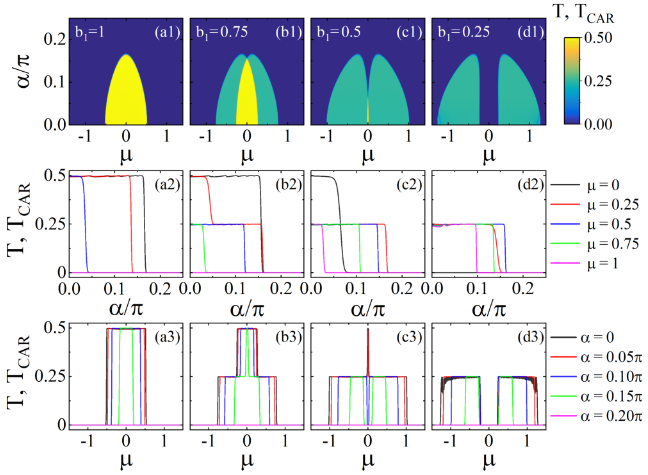

FIG. 3. (a1)–(d1) The transmission coefficient T or the cross Andreev reflection coefficient T_{CAR} as a function of the chemical potential μ and the orientation angle α for different anisotropic distortion parameters b_1 of the hopping strength in the y direction, where $E = 0$, $\Delta_0 = 0.3$, $\Delta_1 = 0$. (a2)–(d2) T or T_{CAR} as a function of α for given μ in (a1)–(d1). (a3)–(d3) T or T_{CAR} as a function of μ for given α in (a1)–(d1).

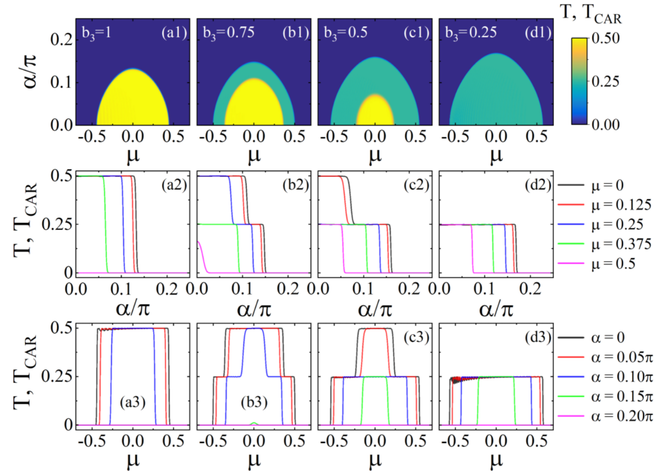

FIG. 4. (a1)–(d1) The transmission coefficient T or the cross Andreev reflection coefficient T_{CAR} as a function of the chemical potential μ and the orientation angle α for different anisotropic distortion parameters b_3 of the superconducting strength in the y direction, where $E = 0$, $b_1 = 1$, $\Delta_0 = 0.4$, $\Delta_1 = 0.3$. (a2)–(d2) T or T_{CAR} as a function of α for given μ in (a1)–(d1). (a3)–(d3) T or T_{CAR} as a function of μ for given α in (a1)–(d1).

consider the case of AMTSC s-wave pairing and the system with crystal anisotropy ($0 < b_1 \leqslant 1$, $\Delta_0 \neq 0$, $\Delta_1 = 0$), as shown in Fig. 3. It is worth noting that, under the current parameters, $T = T_{\mathrm{CAR}}$. From Figs. 3(a1)–3(a3), we can see that T and T_{CAR} exhibit a plateau with the value of 1/2 when $b_1 = 1$. In this case, AM forms a TSC with a vanishing Chern number, possessing two Majorana edge modes of opposite chirality protected by translation symmetry [28]. At the x normal edge, there is one mode each at $k_y = 0$ and $k_y = \pm\pi$, as shown in Fig. 1(d). When μ and α are within an appropriate parameter range, these two pairs of CMES always exist. From the previous analysis, we conclude that $T = T_{\mathrm{CAR}} = 1/2$. However, when α or μ exceeds a certain threshold, both pairs of Majorana edge states will be simultaneously destroyed, resulting in the plateau value suddenly dropping to 0.

When a slight crystal anisotropy is added ($b_1 = 0.75$), as shown in Figs. 3(b1)–3(b3), the original 1/2 plateau splits into two overlapping 1/4 plateaus in the direction of increasing $|\mu|$. In Fig. 3(b1), the plateau value is 1/2 when $|\mu|$ and α are close to zero; as $|\mu|$ and α increase appropriately, the plateau value changes to 1/4. This is because, despite the net magnetization of AM being zero, it can become a chiral TSC with the Chern number $|\mathcal{N}| = 1$ when $b_1 \neq 1$ [28]. At this point, one pair of CMES at $k_y = 0$ or $\pm\pi$ is destroyed, leading to $T = T_{\mathrm{CAR}} = 1/4$. Different signs of μ will disrupt CMES at different k_y values (see SM part D [52] for corresponding bands). As $|\mu|$ and α continue to increase, all CMES are destroyed, and the plateau value drops to 0. In Fig. 3(b2), for different values of μ, the trend of the plateau value as α varies can be categorized into four modes: from 1/2 to 0, from 1/2 to 1/4 to 0, from 1/4 to 0, and remaining at 0, which demonstrates the rich tunability of the plateau value.

When b_1 decreases to 0.5, as shown in Figs. 3(c1)–3(c3), the 1/2 plateau almost completely splits into two 1/4 plateaus. In Fig. 3(c3), the variation trend of the plateau value with $|\mu|$ shows a new mode different from 1/2 to 1/4 to 0, that is, from 0 to 1/4 to 0. Finally, when b_1 decreases to 0.25, as shown in Figs. 3(d1)–3(d3), the two 1/4 plateaus continue to move in the direction of increasing $|\mu|$ and move away from each other, and the 1/2 plateau completely disappears. In addition, there are slight oscillations on the plateau, which are particularly obvious under certain parameters. This is caused by the finite-size effect and the choice of the incident energy $E = 0$ in the numerical calculations. Increasing the junction width W can weaken or even eliminate the oscillations. However, this does not affect our main conclusion: as long as the CMES is not disrupted, the plateau can exist stably.

Then, we consider the case of $s + s_{\pm}$-wave pairing with anisotropic superconducting strength ($b_1 = 1$, $\Delta_{0,1} \neq 0$, $0 < b_3 \leqslant 1$), as shown in Fig. 4. In Figs. 4(a1)–4(a3), T and T_{CAR} also exhibit a 1/2 plateau. This is because, in the case of isotropic $s_{\pm}$ pairing, AM forms a TSC with two pairs CMES similar to s-wave pairing, which results in the plateau value of 1/2.

When there is anisotropy in the superconducting strength ($b_3 \neq 1$), AM also becomes a TSC with the single pair of CMES and the Chern number $|\mathcal{N}| = 1$, which causes the plateau value to be 1/4. From Figs. 4(b1)–4(d1), we observe that, unlike the s-wave pairing, the region corresponding to the 1/2 plateau rapidly shrinks toward $|\mu| = 0$ and $\alpha = 0$. During this process, the original position of the 1/2 plateau is replaced by the 1/4 plateau, whose region gradually expands in the direction opposite to that in which the 1/2 plateau shrinks. Finally, the 1/2 plateau completely disappears, leaving only the 1/4 plateau. This leads to the absence of two variation modes when considering anisotropy compared with s-wave pairing: one is that, at $\mu = 0$, the plateau value no longer changes directly from 1/2 to 0 as α varies; the other is that, as μ varies, the plateau value no longer changes from 0 to 1/4 to 0. The remaining modes are the same as the s-wave pairing. Furthermore, in this case, the platform oscillation is no longer symmetrical about $\mu = 0$. This is because when

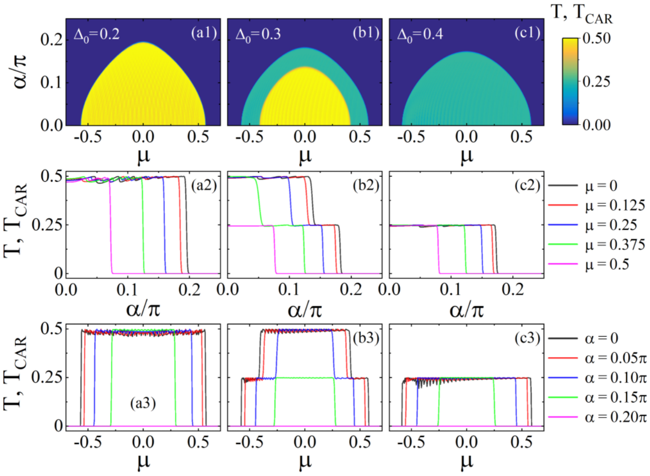

FIG. 5. (a1)–(c1) The transmission coefficient T or the cross Andreev reflection coefficient T_{CAR} as a function of the chemical potential μ and the orientation angle α for different superconducting pairing amplitudes Δ_0 and Δ_1, where $E = 0$, $b_1 = 1$, $\Delta_1 = (\Delta_0 - 0.2)/1.5$, $b_3 = -1$. (a2)–(c2) T or T_{CAR} as a function of α for given μ in (a1)–(c1). (a3)–(c3) T or T_{CAR} as a function of μ for given α in (a1)–(c1).

$\Delta_1 \neq 0$ the momentum of the CMES is related not only to the sign between Δ_0 and Δ_1 (phase difference), but also to the sign of μ (see SM part D [52] for corresponding bands).

The two cases discussed so far both make use of anisotropy. Therefore, anisotropy can serve as a tuning knob for topological superconductivity. Moreover, μ and α can also participate in the adjustment of plateau values and enrich these variations (see SM part D [52] for the bands corresponding to the CMES varying with μ and α).

Finally, we consider the case of $s + d$-wave pairing without anisotropy ($b_1 = 1,\ \Delta_{0,1} \neq 0,\ b_3 = -1$), as shown in Fig. 5. We choose $\Delta_1 = (\Delta_0 - 0.2)/1.5$, this is because when $\Delta_1 \geqslant \Delta_0$ the bulk gap becomes very small or even closes, causing bulk states to participate in transport and thereby destroying the quantized plateau. Therefore, it is necessary to select an appropriate ratio between Δ_0 and Δ_1 (see SM part E [52] for detailed analysis).

We find that even without anisotropy in the system, tunable quantized plateaus can still appear, as shown in Figs. 5(a1)–5(c1). The overall trend in this case is quite similar to $s + s_{\pm}$-wave pairing: as the $\Delta_{0,1}$ increase, the region corresponding to the 1/2 plateau rapidly shrinks toward $|\mu| = 0$ and $\alpha = 0$, and the original position of the 1/2 plateau is replaced by the 1/4 plateau. Unlike $s + s_{\pm}$-wave pairing, the 1/4 plateau slowly shrinks in the same direction as the 1/2 plateau. In Figs. 5(a3)–5(c3), the plateau oscillations are symmetric about $\mu = 0$ when $\Delta_1 = 0$, while the plateau oscillations become asymmetric about $\mu = 0$ when $\Delta_1 \neq 0$. The reason is the same as that discussed previously.

IV. CONCLUSIONS

In summary, the transmission coefficient T and the Andreev reflection coefficient T_{CAR} in the AM/AMTSC/AM junction were investigated. It is found that the heterojunction exhibits a filtering effect, where the vast majority of incident electrons are locally reflected, and only a small portion can pass through the center region of AMTSC. Within an appropriate parameter range, T and T_{CAR} remain equal and exhibit a quantized plateau at the value of $1/2$. By tuning the system parameters, the quantized plateau values can be adjusted to $1/2$, $1/4$, and 0. For the case of s-wave pairing, as the crystal anisotropy increases, the $1/2$ plateau shifts toward larger $|\mu|$ and splits into two $1/4$ plateaus. For the $s + s_{\pm}$-wave pairing, with increasing anisotropy in the superconducting strength, the region corresponding to the $1/2$ plateau rapidly shrinks toward $|\mu| = 0$ and $\alpha = 0$. Meanwhile, the $1/4$ plateau appears in the original position of the $1/2$ plateau and its region slowly expands in the opposite direction to the shrinking of the $1/2$ plateau. Therefore, anisotropy acts as a tuning knob for topological superconductivity. When anisotropy is not considered, in the case of $s + d$-wave pairing, quantized plateaus of T and T_{CAR} can also appear by tuning the superconducting order parameters $\Delta_{0,1}$. Moreover, μ and α can also participate in adjusting the plateau values and enrich these variations. All these phenomena originate from the CMES of the AMTSC and the tunneling between them, which exhibit strong robustness against disorder and can work stably over a wide range of system parameters (see SM part F [52] for the effects of disorder).

ACKNOWLEDGMENTS

This work was supported by the National Natural Science Foundation of China (Grant No. 11874139), the Natural Science Foundation of Hebei province (Grant No. A2019205190), and the Fund of the State Key Laboratory of Low-Dimensional Quantum Physics (Grant No. ZZ202402).

DATA AVAILABILITY

The data that support the findings of this article are not publicly available upon publication because it is not technically feasible and/or the cost of preparing, depositing, and hosting the data would be prohibitive within the terms of this research project. The data are available from the authors upon reasonable request.

[1] J. Krempaský, L. Šmejkal, S. W. D' Souza, M. Hajlaoui, G. Springholz, K. Uhlířová, F. Alarab, P. C. Constantinou, V. Strocov, D. Usanov, *et al.*, Altermagnetic lifting of Kramers spin degeneracy, Nature (London) **626**, 517 (2024).

[2] S. Lee, S. Lee, S. Jung, J. Jung, D. Kim, Y. Lee, B. Seok, J. Kim, B. G. Park, L. Šmejkal, C.-J. Kang, and C. Kim, Broken Kramers degeneracy in altermagnetic MnTe, Phys. Rev. Lett. **132**, 036702 (2024).

[3] X. Zhou, W. Feng, R.-W. Zhang, L. Šmejkal, J. Sinova, Y. Mokrousov, and Y. Yao, Crystal thermal transport in altermagnetic RuO_2, Phys. Rev. Lett. **132**, 056701 (2024).

[4] S.-B. Zhang, L.-H. Hu, and T. Neupert, Finite-momentum Cooper pairing in proximitized altermagnets, Nat. Commun. **15**, 1801 (2024).
[5] J. A. Ouassou, A. Brataas, and J. Linder, Josephson effect in altermagnets, Phys. Rev. Lett. **131**, 076003 (2023).
[6] H. Bai, Y. C. Zhang, Y. J. Zhou, P. Chen, C. H. Wan, L. Han, W. X. Zhu, S. X. Liang, Y. C. Su, X. F. Han, F. Pan, and C. Song, Efficient spin-to-charge conversion via altermagnetic spin splitting effect in antiferromagnet RuO_2, Phys. Rev. Lett. **130**, 216701 (2023).
[7] L. Šmejkal, J. Sinova, and T. Jungwirth, Beyond conventional ferromagnetism and antiferromagnetism: A phase with nonrelativistic spin and crystal rotation symmetry, Phys. Rev. X **12**, 031042 (2022).
[8] I. I. Mazin, Editorial: Altermagnetism—A new punch line of fundamental magnetism, Phys. Rev. X **12**, 040002 (2022).
[9] Y. Guo, H. Liu, O. Janson, I. C. Fulga, J. van den Brink, and J. I. Facio, Spin-split collinear antiferromagnets: A large-scale *ab-initio* study, Mater. Today Phys. **32**, 100991 (2023).
[10] Q. Cheng and Q.-F. Sun, Orientation-dependent Josephson effect in spin-singlet superconductor/altermagnet/spin-triplet superconductor junctions, Phys. Rev. B **109**, 024517 (2024).
[11] Q. Cheng, Y. Mao, and Q.-F. Sun, Field-free Josephson diode effect in altermagnet/normal metal/altermagnet junctions, Phys. Rev. B **110**, 014518 (2024).
[12] M. Papaj, Andreev reflection at the altermagnet-superconductor interface, Phys. Rev. B **108**, L060508 (2023).
[13] C. Sun, A. Brataas, and J. Linder, Andreev reflection in altermagnets, Phys. Rev. B **108**, 054511 (2023).
[14] C. W. J. Beenakker and T. Vakhtel, Phase-shifted Andreev levels in an altermagnet Josephson junction, Phys. Rev. B **108**, 075425 (2023).
[15] N. Read and D. Green, Paired states of fermions in two dimensions with breaking of parity and time-reversal symmetries and the fractional quantum Hall effect, Phys. Rev. B **61**, 10267 (2000).
[16] X.-L. Qi and S.-C. Zhang, Topological insulators and superconductors, Rev. Mod. Phys. **83**, 1057 (2011).
[17] J. Alicea, New directions in the pursuit of Majorana fermions in solid state systems, Rep. Prog. Phys. **75**, 076501 (2012).
[18] C. W. J. Beenakker, Search for Majorana fermions in superconductors, Annu. Rev. Condens. Matter Phys. **4**, 113 (2013).
[19] T. Karzig, C. Knapp, R. M. Lutchyn, P. Bonderson, M. B. Hastings, C. Nayak, J. Alicea, K. Flensberg, S. Plugge, Y. Oreg, C. M. Marcus, and M. H. Freedman, Scalable designs for quasiparticle-poisoning-protected topological quantum computation with Majorana zero modes, Phys. Rev. B **95**, 235305 (2017).
[20] B. Lian, X.-Q. Sun, A. Vaezi, X.-L. Qi, and S.-C. Zhang, Topological quantum computation based on chiral Majorana fermions, Proc. Natl. Acad. Sci. USA **115**, 10938 (2018).
[21] Y.-F. Zhou, Z. Hou, and Q.-F. Sun, Non-Abelian operation on chiral Majorana fermions by quantum dots, Phys. Rev. B **99**, 195137 (2019).
[22] J. D. Sau, R. M. Lutchyn, S. Tewari, and S. Das Sarma, Generic new platform for topological quantum computation using semiconductor heterostructures, Phys. Rev. Lett. **104**, 040502 (2010).
[23] B. Braunecker and P. Simon, Interplay between classical magnetic moments and superconductivity in quantum one-dimensional conductors: Toward a self-sustained topological Majorana phase, Phys. Rev. Lett. **111**, 147202 (2013).
[24] L. Fu and C. L. Kane, Superconducting proximity effect and Majorana fermions at the surface of a topological insulator, Phys. Rev. Lett. **100**, 096407 (2008).
[25] A. R. Akhmerov, J. Nilsson, and C. W. J. Beenakker, Electrically detected interferometry of Majorana fermions in a topological insulator, Phys. Rev. Lett. **102**, 216404 (2009).
[26] D. Zhu, Z.-Y. Zhuang, Z. Wu, and Z. Yan, Topological superconductivity in two-dimensional altermagnetic metals, Phys. Rev. B **108**, 184505 (2023).
[27] Y.-X. Li and C.-C. Liu, Majorana corner modes and tunable patterns in an altermagnet heterostructure, Phys. Rev. B **108**, 205410 (2023).
[28] S. A. A. Ghorashi, T. L. Hughes, and J. Cano, Altermagnetic routes to Majorana modes in zero net magnetization, Phys. Rev. Lett. **133**, 106601 (2024).
[29] A. F. Andreev, The thermal conductivity of the intermediate state in superconductors, Sov. Phys. JETP **19**, 1228 (1964).
[30] K. T. Law, P. A. Lee, and T. K. Ng, Majorana fermion induced resonant Andreev reflection, Phys. Rev. Lett. **103**, 237001 (2009).
[31] Q.-F. Sun, Y.-X. Li, W. Long, and J. Wang, Quantum Andreev effect in two-dimensional HgTe/CdTe quantum well/superconductor systems, Phys. Rev. B **83**, 115315 (2011).
[32] K. Zhang, J. Zeng, Y. Ren, and Z. Qiao, Spin-pairing correlations and spin polarization of Majorana bound states in two-dimensional topological-insulator systems, Phys. Rev. B **96**, 085117 (2017).
[33] J. M. Byers and M. E. Flatté, Probing spatial correlations with nanoscale two-contact tunneling, Phys. Rev. Lett. **74**, 306 (1995).
[34] J. Nilsson, A. R. Akhmerov, and C. W. J. Beenakker, Splitting of a Cooper pair by a pair of Majorana bound states, Phys. Rev. Lett. **101**, 120403 (2008).
[35] M. Veldhorst and A. Brinkman, Nonlocal Cooper pair splitting in a *pSn* junction, Phys. Rev. Lett. **105**, 107002 (2010).
[36] D. Beckmann, H. B. Weber, and H. v. Löhneysen, Evidence for crossed Andreev reflection in superconductor-ferromagnet hybrid structures, Phys. Rev. Lett. **93**, 197003 (2004).
[37] S. Russo, M. Kroug, T. M. Klapwijk, and A. F. Morpurgo, Experimental observation of bias-dependent nonlocal Andreev reflection, Phys. Rev. Lett. **95**, 027002 (2005).
[38] J. Ulrich and F. Hassler, Majorana-assisted nonlocal electron transport through a floating topological superconductor, Phys. Rev. B **92**, 075443 (2015).
[39] S. Das and A. Soori, Crossed Andreev reflection in altermagnets, Phys. Rev. B **109**, 245424 (2024).
[40] Q.-F. Sun, J. Wang, and T.-H. Lin, Resonant Andreev reflection in a normal-metal–quantum-dot–superconductor system, Phys. Rev. B **59**, 3831 (1999).
[41] Q.-F. Sun, H. Guo, and T.-H. Lin, Excess Kondo resonance in a quantum dot device with normal and superconducting leads: The physics of Andreev-normal co-tunneling, Phys. Rev. Lett. **87**, 176601 (2001).

[42] Q.-F. Sun and X. C. Xie, Quantum transport through a graphene nanoribbon–superconductor junction, J. Phys. Condens. Matter **21**, 344204 (2009).

[43] P. G. De Gennes, *Superconductivity of Metals and Alloys* (Benjamin, New York, 1966).

[44] Y. Suzuki, H. Y. Hwang, S.-W. Cheong, and R. B. van Dover, The role of strain in magnetic anisotropy of manganite thin films, Appl. Phys. Lett. **71**, 140 (1997).

[45] C. C. Tsuei and J. R. Kirtley, Pairing symmetry in cuprate superconductors, Rev. Mod. Phys. **72**, 969 (2000).

[46] I. I. Mazin, D. J. Singh, M. D. Johannes, and M. H. Du, Unconventional superconductivity with a sign reversal in the order parameter of $LaFeAsO_{1-x}F_x$, Phys. Rev. Lett. **101**, 057003 (2008).

[47] J. Paglione and R. L. Greene, High-temperature superconductivity in iron-based materials, Nat. Phys. **6**, 645 (2010).

[48] Z. Tang, Y. Chen, Y. Zheng, and X. Luo, Strain engineering magnetocrystalline anisotropy in strongly correlated VTe_2 with room-temperature ferromagnetism, Phys. Rev. B **105**, 214403 (2022).

[49] C. Liu, *et al.*, Understanding epitaxial growth of two-dimensional materials and their homostructures, Nat. Nanotechnol. **19**, 907 (2024).

[50] G. Chen, O. Zilberberg, and W. Chen, Detection of Fermi arcs in Weyl semimetals through surface negative refraction, Phys. Rev. B **101**, 125407 (2020).

[51] Y. Tanaka, B. Lu, and N. Nagaosa, Theory of giant diode effect in d-wave superconductor junctions on the surface of a topological insulator, Phys. Rev. B **106**, 214524 (2022).

[52] See Supplemental Material at http://link.aps.org/supplemental/10.1103/rv94-djlk for (A) the specific form of the discretized Hamiltonian, (B) the effects of system size, (C) the scattering matrix derivation, (D) energy bands under different parameters, (E) the selection of superconducting pairing amplitudes for *sd* wave pairing, and (F) the effects of disorder.

[53] W. Long, Q.-F. Sun, and J. Wang, Disorder-induced enhancement of transport through graphene *p-n* junctions, Phys. Rev. Lett. **101**, 166806 (2008).

[54] Y.-T. Zhang, Z. Hou, X. C. Xie, and Q.-F. Sun, Quantum perfect crossed Andreev reflection in top-gated quantum anomalous Hall insulator-superconductor junctions, Phys. Rev. B **95**, 245433 (2017).

[55] Y.-F. Zhou, H. Jiang, X. C. Xie, and Q.-F. Sun, Two-dimensional lattice model for the surface states of topological insulators, Phys. Rev. B **95**, 245137 (2017).

[56] M. P. L. Sancho, J. M. L. Sancho, and J. Rubio, Quick iterative scheme for the calculation of transfer matrices: Application to Mo(100), J. Phys. F: Met. Phys. **14**, 1205 (1984).

[57] M. P. L. Sancho, J. M. L. Sancho, and J. Rubio, Highly convergent schemes for the calculation of bulk and surface Green functions, J. Phys. F: Met. Phys. **15**, 851 (1985).

[58] J. B. Tjernshaugen, M. Amundsen, and J. Linder, Crossed Andreev reflection revealed by self-consistent Keldysh-Usadel formalism, Phys. Rev. B **110**, 224502 (2024).

[59] S. B. Chung, X.-L. Qi, J. Maciejko, and S.-C. Zhang, Conductance and noise signatures of Majorana backscattering, Phys. Rev. B **83**, 100512(R) (2011).

[60] J. Wang, Q. Zhou, B. Lian, and S.-C. Zhang, Chiral topological superconductor and half-integer conductance plateau from quantum anomalous Hall plateau transition, Phys. Rev. B **92**, 064520 (2015).